Advanced Materials

ADVANCED MATERIALS
www.advmat.de

RESEARCH ARTICLE OPEN ACCESS

Universal Conductance Fluctuations in Quantum Anomalous Hall Insulators

Peng Deng[1,2] | Peng Zhang[3] | Gang Qiu[4] | Ting-Hsun Yang[3] | Chang Niu[5] | Yaochen Li[3] | Wenqiang Cui[1,2] | Yang Feng[1,2] | Peide D. Ye[5] | Ke He[1,6,7] | Kai Chang[1,2] | Kang L. Wang[3]

[1]Beijing Academy of Quantum Information Sciences, Beijing, China | [2]Beijing Key Laboratory of Fault-Tolerant Quantum Computing, Beijing, China | [3]Department of Electrical and Computer Engineering, University of California, Los Angeles, California, USA | [4]Department of Electrical and Computer Engineering, University of Minnesota, Twin Cities, Minnesota, USA | [5]Elmore Family School of Electrical and Computer Engineering, Purdue University, West Lafayette, Indiana, USA | [6]State Key Laboratory of Low Dimensional Quantum Physics, Department of Physics, Tsinghua University, Beijing, China | [7]Hefei National Laboratory, Hefei, China

Correspondence: Peng Deng (dengpeng@baqis.ac.cn) | Yang Feng (fengyang@baqis.ac.cn) | Kai Chang (changkai@baqis.ac.cn) | Kang L. Wang (wang@ee.ucla.edu)

Received: 14 September 2025 | **Revised:** 24 November 2025 | **Accepted:** 19 December 2025

Keywords: magnetic topological insulators | molecular beam epitaxy | quantum anomalous hall effect | quantum interference | universal conductance fluctuations

ABSTRACT

Universal conductance fluctuations (UCF) are a distinctive mesoscopic transport phenomenon that arises in disordered systems when the sample size approaches the phase coherence length of the system. As a hallmark of phase coherent transport, UCF shapes the low temperature transport properties of such systems in a fundamental way. In this study, UCF are reported in magnetically doped topological insulator thin films in the quantum anomalous Hall (QAH) regime. In mesoscopic QAH devices, aperiodic yet highly reproducible conductance fluctuations are observed, robust against variations in field sweeping direction and temperature. Two fluctuation components with distinct characteristic frequencies are revealed, and their contrasting temperature dependencies indicate that they originate from different interference processes associated with bulk and edge states, respectively. These finding uncovers rich quantum interference phenomena in the QAH insulators, providing new insights into mesoscopic transport in QAH systems.

1 | Introduction

Quantum anomalous Hall (QAH) insulator is a novel state of matter arising from the interplay between nontrivial band topology and broken time-reversal symmetry [1–7]. In QAH insulators, chiral edge states propagate unidirectionally along the sample boundary, giving rise to a quantized Hall resistance and vanishing longitudinal resistance, even in the absence of an external magnetic field. The QAH effect was first experimentally realized in magnetically doped topological insulators [3–6, 8] and has since been observed in a growing family of systems, ranging from antiferromagnetic topological insulators $MnBi_2Te_4$ [9] to twisted bilayer graphene [10] and $MoTe_2/WSe_2$ heterostructures [11]. More recently, the fractional QAH effect has been realized in twisted $MoTe_2$ [12, 13] and multilayer graphene [14]. QAH insulators provide a versatile platform for exploring a wide range of exotic quantum phases and phenomena, including axion insulator, high-Chern-number QAH insulators, Weyl semimetals, and topological superconductivity [15–27]. Beyond their fundamental interest, QAH insulators hold great promise for applications. The dissipationless edge states open a pathway toward low-power-consumption electronics, while the precisely quantized Hall resistance provides a robust standard for electrical resistance metrology [28–30]. Moreover, when coupled to s-wave supercon-

ductors, QAH systems can host chiral Majorana modes [31] or Majorana zero modes [32, 33], which are essential ingredients for fault-tolerant quantum computing [34, 35].

To fully unlock these applications, it is crucial to understand the transport properties of QAH systems at the mesoscopic scale, the scale at which practical devices ultimately operate. Intriguingly, mesoscopic QAH systems often display transport behaviors that are markedly from their macroscopic counterparts [36–38]. In the mesoscopic regime, quantum interference plays a central role in shaping electronic dynamics [39]. A particular direct manifestation of this interference is the universal conductance fluctuations (UCF), [40–42] which arise in disordered systems as electrons scatter coherently from impurities while traversing the material. In such disordered landscapes, electrons traveling between two points can follow multiple possible paths, and the quantum interference among these paths does not average out in mesoscopic devices, leading to aperiodic yet reproducible conductance fluctuations as a function of magnetic field. These sample-specific fluctuations remain stable as long as the impurity configuration is unchanged, and are therefore referred to as the magneto-fingerprint of the sample. Historically, UCF has been a powerful tool for investigating quantum interference and dephasing mechanisms across a wide variety of material systems, including metals [43], semiconductor nanowires [44, 45], quantum dots [46], quantum Hall devices [47–49], graphene [50–52], and topological materials [53–56]. Yet in QAH materials, UCF remains largely unexplored. Investigating these interference effects in QAH insulators is not only essential for optimizing device performance but also for advancing our understanding of the underlying dephasing mechanisms.

2 | Results

2.1 | Basic Characterization of the QAH Effect

In this work, we report the observation of UCF in a QAH system realized in the magnetically doped topological insulator Cr-doped $(Bi,Sb)_2Te_3$ (CBST). The 5-quintuple-layer (QL) CBST films were grown on semi-insulating GaAs(111)B substrates using molecular beam epitaxy (MBE), following procedures described in our previous reports [17, 20, 36]. From the same batch of 5-QL CBST films, we fabricate four Hall bar devices with widths of 500, 200, 100, and 50 μm, all with a fixed length-to-width ratio of 2, for transport measurements. Figure 1b,c presents the field dependence of the longitudinal resistivity (ρ_{xx}) and Hall resistivity (ρ_{yx}), respectively, for the 500 μm-wide Hall bar device. The corresponding longitudinal conductance (σ_{xx}) and Hall conductance (σ_{xy}), obtained using the tensor relationship $\sigma_{xx} = \rho_{xx}/(\rho_{xx}^2 + \rho_{yx}^2)$ and $\sigma_{xy} = \rho_{yx}/(\rho_{xx}^2 + \rho_{yx}^2)$, are shown in Figure 1d,e, respectively. At the base temperature, the device exhibits a nearly perfectly quantized Hall resistivity ($|\rho_{yx}| > 0.9997\, h/e^2$, where h is the Planck constant and e is the elementary charge) and a vanishing longitudinal resistivity ($\rho_{xx} < 2.5 \times 10^{-3}\ h/e^2$) in the fully magnetized state (Figure 1f), hallmark signatures of the QAH effect. Similar quantization conditions are also observed in the 200, 100, and 50 μm devices, as shown in Figure S2.

The exchange gap Δ is extracted by fitting the temperature dependence of σ_{xx} to the Arrhenius law $\sigma_{xx} \sim \exp(-T_0/T)$, wherein $\Delta = k_B T_0$. The fitted T_0 values are 1.31, 2.03, 2.11, and 1.79 K for the 500, 200, 100, and 50 μm devices, respectively. It is worth noting that the 500 μm device is patterned using a hard mask, whereas the others were fabricated via photolithography. The slightly higher T_0 values in the latter may result from a Fermi level shift induced during the fabrication process.

The QAH effect remains robust under high magnetic fields, which is the regime of primary interest in the following discussion. Figure 2 presents the field dependence of ρ_{xx} and ρ_{yx} for all four devices, measured at 50 mK up to 12 T. Across the entire field range, except for a narrow window at around the coercive field, ρ_{xx} stays negligibly small, while ρ_{yx} remains quantized. In particular, as the field is ramped from 1 to 12 T, the change in ρ_{xx} is below $7.0 \times 10^{-4}\ h/e^2$ for all devices. These minimal variations underscore the remarkable stability of the QAH state even under strong magnetic fields.

2.2 | UCF in Mesoscopic QAH Devices

After confirming the presence of the QAH state in all four devices of different widths, we turn to investigate UCF in these systems. To this end, we examine σ_{2T}, defined as the inverse of the two-terminal resistance R_{2T}. The four-probe measurement configuration for R_{2T} is schematically illustrated in the inset of Figure 3a. In this setup, voltage probes on opposite sides of the Hall bar, specifically, probes 2 and 6, as well as probes 3 and 5, are shorted on-chip, respectively. The current is applied between probes 1 and 4, and R_{2T} is defined as the resistance between these two shorted pairs. This configuration allows UCF to be observed in much larger devices, as explained below, hence bypassing the need for electron-beam lithography in device fabrication, which can damage the sample and degrade its quality [57]. In this geometry, σ_{2T} corresponds to the two-terminal conductance of the Hall bar, which, according to the Landauer-Büttiker formalism, is expected to take a quantized value of e^2/h.

Figure 3a presents the field dependence of σ_{2T} for all four devices, measured with a 100 nA current (corresponding raw R_{2T} data are shown in Figure S3). In the 500 and 200 μm devices, σ_{2T} displays a quantized value. In stark contrast, the 100 and 50 μm devices exhibit significant deviation from the Landauer-Buttiker ideal, with σ_{2T} exceeding e^2/h. Notably, aperiodic conductance fluctuations are observed in two smaller devices. These fluctuations are reproducible in the forward and backward field sweeps, indicating that they arise from intrinsic quantum interference effects rather than measurement noise.

The deviation of σ_{2T} from the quantized value in the 100 and 50 μm devices can be attributed to electric breakdown in QAH insulators [58–60]. The quantized condition, $\sigma_{2T} = e^2/h$, is realized when the counter-propagating chiral edge states on opposite sides of the sample do not hybridize. However, when the transverse electric field exceeds a critical threshold, electrons gain sufficient energy to tunnel from one edge to the other edge, resulting in $\sigma_{2T} > e^2/h$. This breakdown process is further facilitated by charge puddles that are inevitably formed in the magnetically doped topological insulators [60]. Because smaller devices experience larger electric

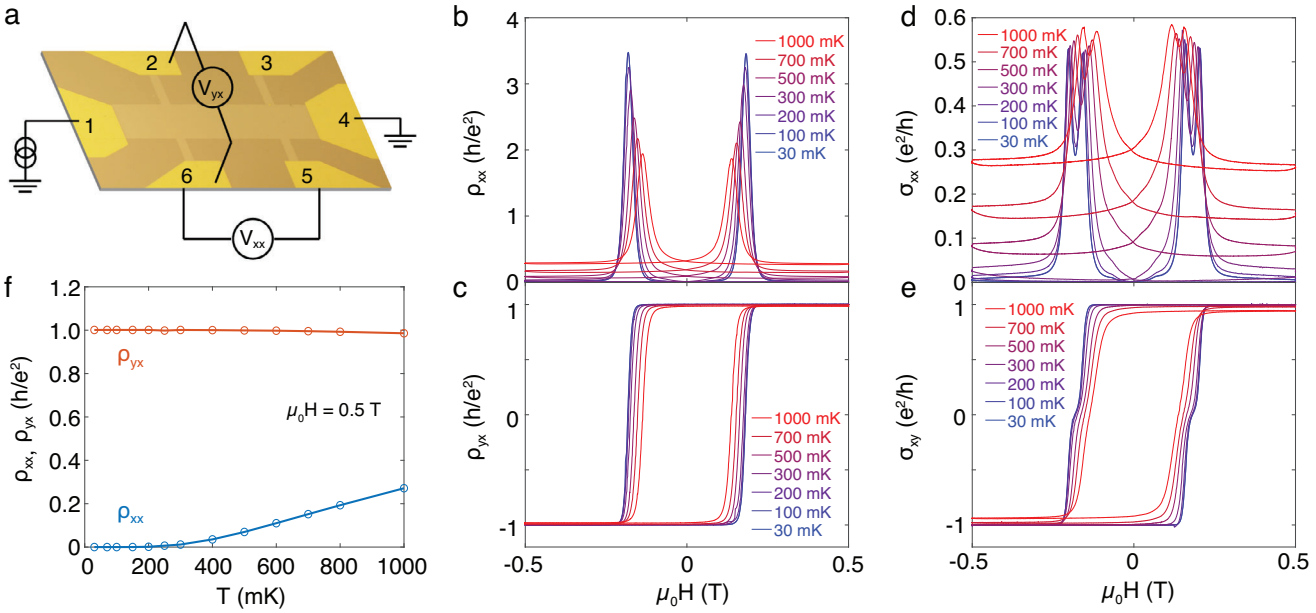

FIGURE 1 | QAH effect in the 5-QL-CBST. (a) Schematic of measurement setup. (b,c) Field dependence of ρ_{xx} and ρ_{yx} at different temperatures for the 5-QL-CBST sample. (d,e) Field dependence of σ_{xx} and σ_{xy} for the same sample. f) Temperature dependence of the ρ_{xx} and ρ_{yx}.

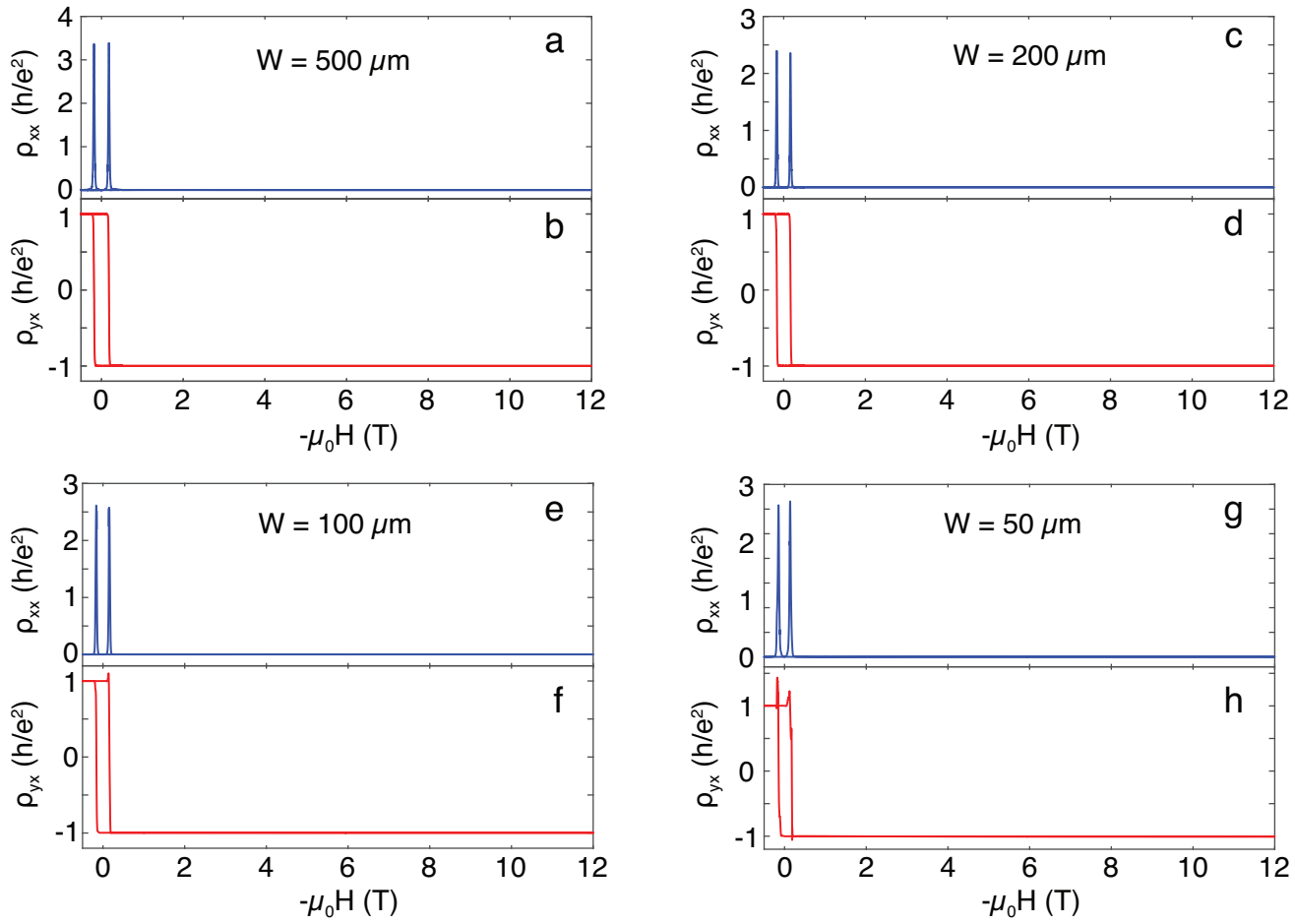

FIGURE 2 | QAH effect in high magnetic field. Field dependence of ρ_{xx} and ρ_{yx} for the (a,b) 500 μm, (c,d) 200 μm, (e,f) 100 μm, and (g,h) 50 μm devices. All curves are measured at 50 mK. An excitation current of 100 nA is sourced for all four devices.

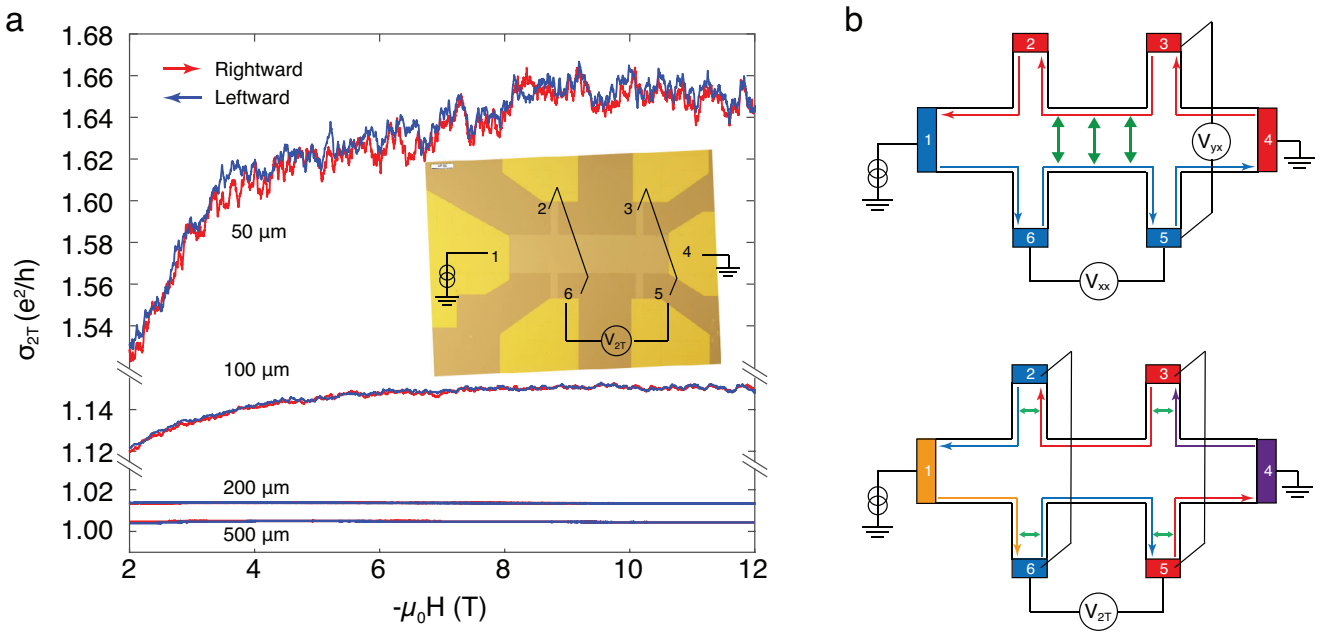

FIGURE 3 | UCF in QAH devices. (a) Field dependence of σ_{2T} for QAH devices with different widths. All measurements were performed at 50 mK with an excitation current of 100 nA. Inset: schematics of measurement setup for two-terminal resistances R_{2T}. (b) Schematics of electrical breakdown in ρ_{xx}/ρ_{yx} (upper panel) and σ_{2T} (lower panel) measurement configurations. The electrodes and edges at equal potential are highlighted by the same color, and regions where electrical breakdown occurs are denoted by green arrows.

fields under the same applied current, electrical breakdown appears only in two smaller devices, with the effect being more pronounced in the 50 μm device. To further illustrate this point, we examine the field dependence of σ_{2T} under different excitation currents. As shown in Figure S4, σ_{2T} increases monotonically with increasing current.

We would like to note that the electrical breakdown is more readily observed in the σ_{2T} measurement configuration (inset of Figure 3a) than in the conventional ρ_{xx}/ρ_{yx} measurement setup (Figure 1a). As illustrated in Figure 3b, in the ρ_{xx}/ρ_{yx} setup, the Hall probes on both sides of the Hall bar are at equal potential to the source and drain, respectively, so the voltage drop occurs across the full width of the Hall bar. In contrast, in the σ_{2T} measurement, probes 2 and 6, as well as 3 and 5, are shorted on the chip, and the voltage drop is instead concentrated over a much narrower region across the width of the Hall probes (see Experimental Section for the specific width of Hall probes for four QAH devices). This more localized voltage drop produces a significantly larger electric field for the same applied current, causing electrical breakdown to occur at a much lower current in the σ_{2T} configuration.

2.3 | Origin of UCF

Next, we focus on the UCF in the 50 μm device. To better visualize these fluctuations, $\Delta\sigma_{2T}$ is obtained by subtracting a polynomial background from σ_{2T}. The magnetic field dependence of $\Delta\sigma_{2T}$ at different temperatures is presented in Figure 4a, where reproducible features are observed across multiple scans. This strong reproducibility further confirms that the fluctuations arise from quantum interference of electron trajectories rather than measurement noise. Notably, these fluctuations exhibit quasi-periodic behaviors, with dominant frequencies set by the characteristic sizes of the areas enclosed by the interference paths.

To further analyze these fluctuations, we applied fast Fourier transforms (FFT) to the data. Figure 4b,c show that the Fourier spectra behave differently at base and elevated temperatures. At 50 mK, a prominent peak appears around 6.0 T^{-1}, corresponding to a periodicity of ΔB = 166.6 mT, alongside low-frequency components. This peak gradually diminishes as temperature increases (Figure S5) and is entirely absent at 1300 mK spectrum, where only low-frequency fluctuations remain. The contrasting temperature dependence of high- and low-frequency components is also evident in Figure 4a: the slowly varying background persists at all temperatures, while the faster, noise-like features are progressively smooth out as the temperature increases.

To separate the high- and low-frequency fluctuations, high- and low-pass filters are applied to the Fourier spectra using a cutoff frequency (e.g., f_c = 5 T^{-1}) chosen between their characteristic frequency ranges. Note that the choice of f_c does not qualitatively affect the results discussed below. The filtered spectra are then subjected to inverse Fourier transforms, yielding $\Delta\sigma_H$ and $\Delta\sigma_L$, corresponding to the high- and low-frequency contributions, respectively.

Figure 5a shows the field dependence of $\Delta\sigma_H$ at various temperatures, with a zoomed-in plot provided in Figure 5b highlighting the visual similarities across different scans. The magnitude of the fluctuation, quantified by the root mean square of $\Delta\sigma_H$, $\Delta\sigma_H^{rms}$, decreases with increasing temperature, as shown in Figure 5c. The field dependence of $\Delta\sigma_L$ is shown in Figure 5d, where highly reproducible features are also evident. Interestingly, the

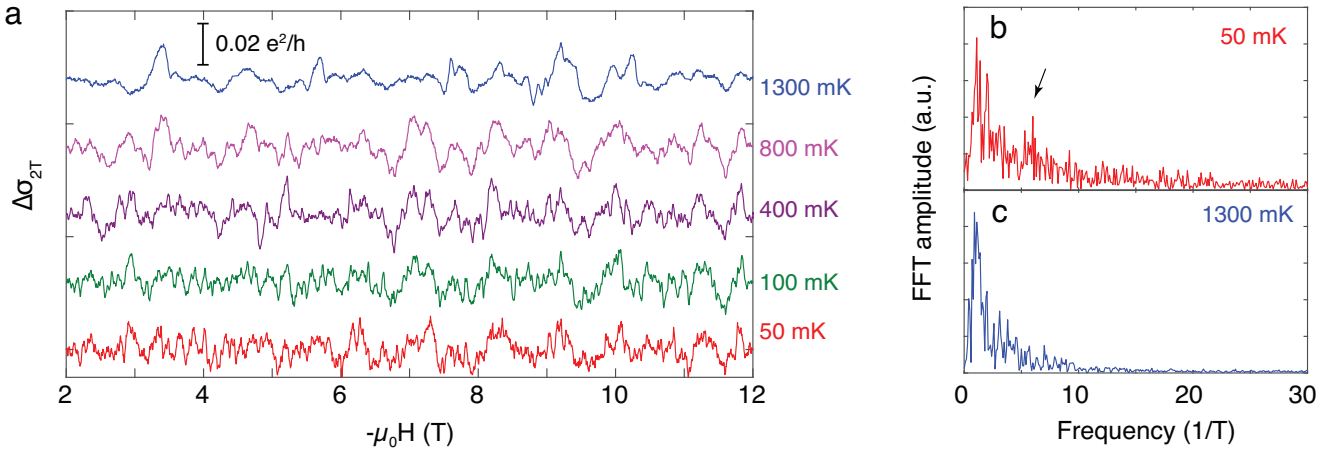

FIGURE 4 | UCF under different temperatures. (a) Field dependence of $\Delta\sigma_{2T}$ for the 50 μm devices at different temperatures. (b,c) Fast Fourier transform of $\Delta\sigma_{2T}$ at 50 and 1300 mK, respectively. The black arrow indicates the frequency corresponding to the high-frequency fluctuations.

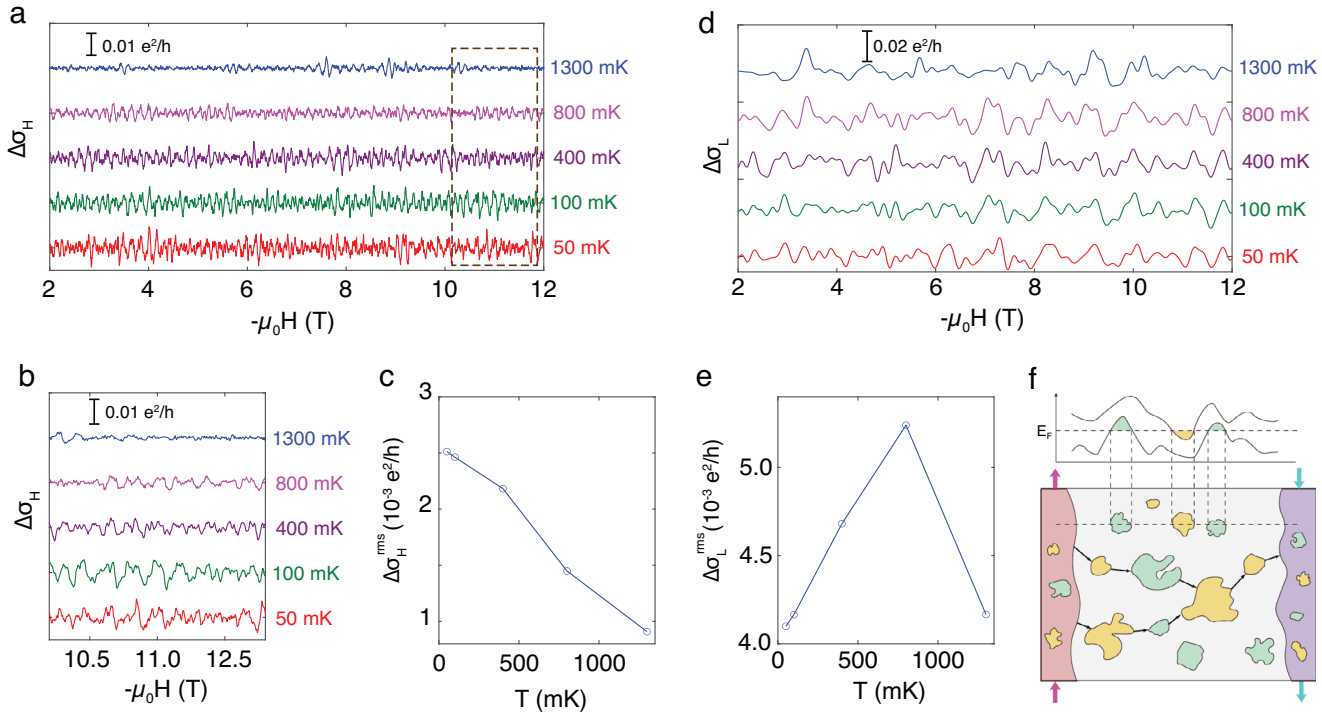

FIGURE 5 | The high- and low-frequency fluctuations. (a) Field dependence of high-frequency fluctuations $\Delta\sigma_H$ at different temperatures. (b) Zoomed-in plot of the region highlighted by the dashed box in (a). (c) Temperature dependence of $\Delta\sigma_H^{rms}$. (d) Field dependence of low-frequency fluctuations $\Delta\sigma_L$ at different temperatures. (e) Temperature dependence of $\Delta\sigma_L^{rms}$. (f) Schematics of the interference associated with high- and low-frequency fluctuations. The yellow and green regions denote the electron and hole puddles, respectively.

corresponding root mean square $\Delta\sigma_L^{rms}$ displays a non-monotonic temperature dependence, initially increasing and then decreasing as the temperature decreases (Figure 5e).

The distinct temperature dependence of the low- and high-frequency components apparently suggests that they originate from different interference processes. In the electrical breakdown regime where UCF is observed, electrons traverse the bulk of the sample, moving from the edge at a higher chemical potential to that at a lower chemical potential. In magnetically doped topological insulators, the energy landscape is modulated by spatial variations in electrostatic potential [61–64], as well as the fluctuations in the local exchange gap arising from the random distribution of magnetic dopants [65]. Together, these inhomogeneities give rise to the formation of charge puddles, as schematically illustrated in Figure 5f. As electrons propagate through this inhomogeneous landscape, their trajectories can form closed loops encircling these charge puddles. The characteristic frequency of the fluctuation enables an estimation of the average size of the charge puddles via the relationship:

$\Delta B\pi r^2 = \Phi_0$, where Φ_0 is the magnetic flux quanta and r is the puddle radius. For the high-frequency fluctuations, which exhibit a dominant periodicity of ΔB = 166.6 mT, this corresponds to an average size of $r \approx 63$ nm, in good agreement with scanning tunneling microscopy results [63, 64]. These high-frequency fluctuations are therefore attributed to the interference of bulk currents, and they diminish at higher temperatures due to the reduction in phase coherence length.

By contrast, the low-frequency fluctuations exhibit a markedly different temperature dependence. Their behavior suggests that they may be associated with interference processes involving the chiral edge states. Although the exact spatial profile of chiral edge states remains under investigation, growing evidence indicates that they are not strictly confined to the sample boundary but instead extend into the bulk over a finite width [38, 66, 67]. This finite-width region exhibits an enhanced local density of state and metallic character, resembling the compressible region in the QH effect. In both cases, such an extended region supports the flow of chiral edge channels. In such a region, electrons can form interference loops that contribute to conductance fluctuations. As the temperature decreases, chiral edge states become more localized, effectively narrowing the width of the compressible region and thereby reducing the fluctuation amplitude. At elevated temperatures, on the other hand, enhanced dephasing also suppresses the quantum interference. Together, these effects give rise to the non-monotonic temperature dependence observed for $\Delta\sigma_L^{rms}$. Moreover, that $\Delta\sigma_L^{rms}$ exceeds $\Delta\sigma_H^{rms}$ indicates the interference response for the low-frequency fluctuations occurs within a more spatially confined region, further supporting its edge state origin.

The amplitude of the conductance fluctuations also allows an estimate of the phase coherence length L_ϕ via the relationship: $\Delta\,\sigma_{2T}^{rms} = \frac{e^2}{h}\,(\frac{L_\phi}{L})^{3/2}$. At 50 mK, we obtain a coherence length of $L_\phi \approx 1.4$ µm. This length scale is comparable to those obtained from previous studies of QAH insulators realized in magnetically doped topological insulators [36, 59], where L_ϕ was determined using different approaches. The consistency between these estimates indicates that various phase coherent phenomena arise from interference occurring over regions of similar characteristic size.

The distinct temperature dependences of the high- and low-frequency fluctuations are also evidenced in the 100 µm device (Figure S6). In this larger device, the overall fluctuation amplitude is reduced, as is expected for a general interference effect. Notably, however, $\Delta\sigma_H^{rms}$ exhibits a much stronger relative reduction than $\Delta\sigma_L^{rms}$, highlighting their distinct origins associated with bulk and edge states, respectively.

Finally, we compare the conductance fluctuations observed in this work with those reported in our previous study [37], where similar conductance fluctuations in submicron-sized QAH devices were attributed to interference paths encircling magnetic domains. Although similar fluctuations are observed in both studies, several key differences distinguish the two cases. First, the fluctuations in [37] appear only near the coercive field (~ 0.2 T), where a large number of magnetic domains are present, whereas the fluctuations reported here persist up to 12 T, deep in the single-domain regime. Second, the earlier fluctuations are generally less reproducible across different field sweeps, reflecting the stochastic nature of domain formation during the magnetization reversal process. In contrast, the fluctuations in our devices are highly reproducible, consistent with their origin in static charge puddles set by quenched disorder. Finally, the characteristic size of the area enclosed by the interference loops differs: it is set by magnetic domain size in [37] and by charge puddles in our case, which are approximately four times smaller in diameter.

3 | Conclusion

To summarize, we investigate UCF in QAH systems realized in the magnetically doped topological insulators Cr-doped $(Bi, Sb)_2Te_3$. In mesoscopic devices, we observed reproducible conductance fluctuations in the two-terminal conductance σ_{2T}. Two distinct types of fluctuations, differing in frequency and temperature dependence, are identified, pointing to separate underlying interference processes: the high-frequency component arises from bulk current loops around charge puddles, whereas the low-frequency component originates from interference of chiral edge states. These findings offer new insights into the quantum interference in QAH materials, which are essential for advancing QAH-based low-power-consumption electronics and quantum computing technologies.

4 | Experimental Section

4.1 | MBE Growth and Characterizations

The epitaxy growth of Cr-doped $(Bi,Sb)_2Te_3$ was conducted in an MBE system with a base vacuum rate of 5×10^{-10} Torr. Epi-ready semi-insulating GaAs(111)B wafers were used as the substrate. Prior to growth, GaAs substrates were annealed at up to 680°C under a Te-rich environment. During growth, substrates were held at 180°C and high-purity Cr (99.995%), Bi (99.999%), Sb (99.999%), and Te (99.9999%) were deposited on the substrate. The growth was in situ monitored by reflective high-energy electron diffraction (RHEED). The thickness of the sample was calibrated by the oscillation of RHEED intensity.

4.2 | Device Fabrication and Transport Measurements

Grown films were patterned into Hall bar devices for transport measurement. The 500 µm-wide devices were defined using stencil masks, while the 200, 100, and 50 µm-wide devices were patterned by photolithography. All devices have a fixed length-to-width ratio of 2 for all devices. The widths of the Hall probe, which are the relevant length scales for electrical breakdown in the σ_{2T} measurement configuration, are 500, 40, 20, and 10 µm, for the 500, 200, 100, and 50 µm wide Hall bar devices, respectively. All devices were dry-etched using CHF_3. Indium contacts were used for devices patterned via hard masks, and Cr/Au (20/ 80 nm) contacts were used for the photolithographically patterned devices. Transport measurements were carried out in a dilution refrigerator (Oxford Instruments). A low-frequency AC

current was sourced (Keithley 6221) and the voltage was picked up by lock-in amplifiers (Stanford Research System SR830).

Author Contributions

P.D., Y.F., K.C. and K.L.W. conceived the research. P.D., P.Z., G.Q. and W.C. performed sample growth and device fabrication. P.D., P.Z., G.Q., T.-H.Y. and Y.L. performed transport measurements with the help of C.N. and P.D.Y., P.D., W.C., Y.F., K.H. and K.C. analyzed the data. P.D. wrote the manuscript with the inputs from all authors.

Acknowledgements

This work was supported by Quantum Science and Technology-National Science and Technology Major Project (No. 2023ZD0300500), National Natural Science Foundation of China (Nos. 12304189, 92165104, 12074038, 92365201 and 12474497), Beijing Natural Science Foundation (No. 1232035), and Beijing Municipal Science & Technology Commission (No. Z221100002722013).

Conflicts of Interest

The authors declare no conflicts of interest.

Data Availability Statement

The data that support the findings of this study are available from the corresponding author upon reasonable request.

References

1. F. D. M. Haldane, "Model for a Quantum Hall Effect without Landau Levels: Condensed-matter Realization of the" Parity Anomaly," *Physical Review Letters* 61 (1988): 2015.

2. R. Yu, W. Zhang, H.-J. Zhang, S.-C. Zhang, X. Dai, and Z. Fang, "Quantized Anomalous Hall Effect in Magnetic Topological Insulators," *Science* 329 (2010): 61–64.

3. C.-Z. Chang, J. Zhang, X. Feng, et al., "Experimental Observation of the Quantum Anomalous Hall Effect in a Magnetic Topological Insulator," *Science* 340 (2013): 167–170, https://doi.org/10.1126/science.1234414.

4. X. Kou, S.-T. Guo, Y. Fan, et al., "Scale-Invariant Quantum Anomalous Hall Effect in Magnetic Topological Insulators beyond the Two-Dimensional Limit," *Physical Review Letters* 113 (2014): 137201, https://doi.org/10.1103/PhysRevLett.113.137201.

5. J. Checkelsky, R. Yoshimi, A. Tsukazaki, et al., "Trajectory of the Anomalous Hall Effect towards the Quantized state in a Ferromagnetic Topological Insulator," *Nature Physics* 10 (2014): 731–736, https://doi.org/10.1038/nphys3053.

6. A. Kandala, A. Richardella, S. Kempinger, C.-X. Liu, and N. Samarth, "Giant Anisotropic Magnetoresistance in a Quantum Anomalous Hall Insulator," *Nature Communications* 6 (2015): 7434, https://doi.org/10.1038/ncomms8434.

7. C.-Z. Chang, C.-X. Liu, and A. H. MacDonald, "Colloquium: Quantum Anomalous Hall Effect," *Reviews of Modern Physics* 95 (2023): 011002, https://doi.org/10.1103/RevModPhys.95.011002.

8. C.-Z. Chang, W. Zhao, D. Y. Kim, et al., "High-precision Realization of Robust Quantum Anomalous Hall state in a Hard Ferromagnetic Topological Insulator," *Nature Materials* 14 (2015): 473–477, https://doi.org/10.1038/nmat4204.

9. Y. Deng, Y. Yu, M. Z. Shi, et al., "Quantum Anomalous Hall Effect in Intrinsic Magnetic Topological Insulator $MnBi_2Te_4$," *Science* 367 (2020): 895–900, https://doi.org/10.1126/science.aax8156.

10. M. Serlin, C. Tschirhart, H. Polshyn, et al., "Intrinsic Quantized Anomalous Hall Effect in a Moiré Heterostructure," *Science* 367 (2020): 900–903, https://doi.org/10.1126/science.aay5533.

11. T. Li, S. Jiang, B. Shen, et al., "Quantum Anomalous Hall Effect from Intertwined Moiré Bands," *Nature* 600 (2021): 641–646, https://doi.org/10.1038/s41586-021-04171-1.

12. H. Park, J. Cai, E. Anderson, et al., "Observation of Fractionally Quantized Anomalous Hall Effect," *Nature* 622 (2023): 74–79, https://doi.org/10.1038/s41586-023-06536-0.

13. F. Xu, Z. Sun, T. Jia, et al., "Observation of Integer and Fractional Quantum Anomalous Hall Effects in Twisted Bilayer $MoTe_2$," *Physical Review X* 13 (2023): 031037.

14. Z. Lu, T. Han, Y. Yao, et al., "Fractional Quantum Anomalous Hall Effect in Multilayer Graphene," *Nature* 626 (2024): 759–764, https://doi.org/10.1038/s41586-023-07010-7.

15. X.-L. Qi, T. L. Hughes, and S.-C. Zhang, "Topological Field Theory of Time-reversal Invariant Insulators," *Physical Review B* 78 (2008): 195424, https://doi.org/10.1103/PhysRevB.78.195424.

16. M. Mogi, M. Kawamura, R. Yoshimi, et al., "A Magnetic Heterostructure of Topological Insulators as a Candidate for an Axion Insulator," *Nature Materials* 16 (2017): 516–521, https://doi.org/10.1038/nmat4855.

17. P. Deng, Y. Han, P. Zhang, S. K. Chong, Z. Qiao, and K. L. Wang, "Tuning the Number of Chiral Edge Channels in a Fixed Quantum Anomalous Hall System," *Physical Review B* 109 (2024): L201402.

18. Y.-F. Zhao, R. Zhang, R. Mei, et al., "Tuning the Chern Number in Quantum Anomalous Hall Insulators," *Nature* 588 (2020): 419–423, https://doi.org/10.1038/s41586-020-3020-3.

19. I. Belopolski, R. Watanabe, Y. Sato, et al., "Synthesis of a Semimetallic Weyl Ferromagnet with Point Fermi Surface," *Nature* 637 (2025): 1078–1083, https://doi.org/10.1038/s41586-024-08330-y.

20. P. Deng, P. Zhang, C. Eckberg, et al., "Quantized Resistance Revealed at the Criticality of the Quantum Anomalous Hall Phase Transitions," *Nature Communications* 14 (2023): 5558, https://doi.org/10.1038/s41467-023-40784-y.

21. P. Zhang, P. P. Balakrishnan, C. Eckberg, et al., "Exchange-Biased Quantum Anomalous Hall Effect," *Advanced Materials* 35 (2023): 2300391, https://doi.org/10.1002/adma.202300391.

22. C. Niu, J.-P. Hanke, P. M. Buhl, et al., "Mixed Topological Semimetals Driven by Orbital Complexity in Two-dimensional Ferromagnets," *Nature Communications* 10 (2019): 3179, https://doi.org/10.1038/s41467-019-10930-6.

23. C. Niu, N. Mao, X. Hu, B. Huang, and Y. Dai, "Quantum Anomalous Hall Effect and Gate-controllable Topological Phase Transition in Layered $EuCd_2As_2$," *Physical Review B* 99 (2019): 235119, https://doi.org/10.1103/PhysRevB.99.235119.

24. X. Feng, Y. Bai, Z. Chen, Y. Dai, B. Huang, and C. Niu, "Engineering Quantum Anomalous Hall Effect with a High Chern Number in Nonmagnetic Second-Order Topological Insulator," *Advanced Functional Materials* 35 (2025): 2501934, https://doi.org/10.1002/adfm.202501934.

25. A. Uday, G. Lippertz, K. Moors, et al., "Induced Superconducting Correlations in a Quantum Anomalous Hall Insulator," *Nature Physics* 20 (2024): 1589–1595, https://doi.org/10.1038/s41567-024-02574-1.

26. Y. Choi, Y. Choi, M. Valentini, et al., "Superconductivity and Quantized Anomalous Hall Effect in Rhombohedral Graphene," *Nature* 639 (2025): 342–347, https://doi.org/10.1038/s41586-025-08621-y.

27. H. Yi, Y.-F. Zhao, Y.-T. Chan, et al., "Interface-induced Superconductivity in Magnetic Topological Insulators," *Science* 383 (2024): 634–639.

28. Y. Okazaki, T. Oe, M. Kawamura, et al., "Quantum Anomalous Hall Effect with a Permanent Magnet Defines a Quantum Resistance Standard," *Nature Physics* 18 (2022): 25–29, https://doi.org/10.1038/s41567-021-01424-8.

29. D. Patel, K. Fijalkowski, M. Kruskopf, et al., "A Zero External Magnetic Field Quantum Standard of Resistance at the 10^{-9} Level," *Nature Electronics* 7 (2024): 1111–1116, https://doi.org/10.1038/s41928-024-01295-w.

30. N. J. Huáng, J. L. Boland, K. M. Fijalkowski, et al., "Quantum Anomalous Hall Effect for Metrology," *Applied Physics Letters* 126 (2025): 040501, https://doi.org/10.1063/5.0233689.

31. J. Wang, Q. Zhou, B. Lian, and S.-C. Zhang, "Chiral Topological Superconductor and Half-integer Conductance Plateau from Quantum Anomalous Hall Plateau Transition," *Physical Review B* 92 (2015): 064520, https://doi.org/10.1103/PhysRevB.92.064520.

32. C.-Z. Chen, Y.-M. Xie, J. Liu, P. A. Lee, and K. T. Law, "Quasi-one-dimensional Quantum Anomalous Hall Systems as New Platforms for Scalable Topological Quantum Computation," *Physical Review B* 97 (2018): 104504, https://doi.org/10.1103/PhysRevB.97.104504.

33. Y. Zeng, C. Lei, G. Chaudhary, and A. H. MacDonald, "Quantum Anomalous Hall Majorana Platform," *Physical Review B* 97 (2018): 081102, https://doi.org/10.1103/PhysRevB.97.081102.

34. A. Y. Kitaev, "Fault-tolerant Quantum Computation by Anyons," *Annals of Physics* 303 (2003): 2–30, https://doi.org/10.1016/S0003-4916(02)00018-0.

35. C. Nayak, S. H. Simon, A. Stern, M. Freedman, and S. D. Sarma, "Non-Abelian Anyons and Topological Quantum Computation," *Reviews of Modern Physics* 80 (2008): 1083–1159, https://doi.org/10.1103/RevModPhys.80.1083.

36. P. Deng, C. Eckberg, P. Zhang, et al., "Probing the Mesoscopic Size Limit of Quantum Anomalous Hall Insulators," *Nature Communications* 13 (2022): 4246, https://doi.org/10.1038/s41467-022-31105-w.

37. G. Qiu, P. Zhang, P. Deng, et al., "Mesoscopic Transport of Quantum Anomalous Hall Effect in the Submicron Size Regime," *Physical Review Letters* 128 (2022): 217704, https://doi.org/10.1103/PhysRevLett.128.217704.

38. L.-J. Zhou, R. Mei, Y.-F. Zhao, et al., "Confinement-Induced Chiral Edge Channel Interaction in Quantum Anomalous Hall Insulators," *Physical Review Letters* 130 (2023): 086201, https://doi.org/10.1103/PhysRevLett.130.086201.

39. J.-J. Lin and J. Bird, "Recent Experimental Studies of Electron Dephasing in Metal and Semiconductor Mesoscopic Structures," *Journal of Physics: Condensed Matter* 14 (2002): R501, https://doi.org/10.1088/0953-8984/14/18/201.

40. P. A. Lee and A. D. Stone, "Universal Conductance Fluctuations in Metals," *Physical Review Letters* 55 (1985): 1622, https://doi.org/10.1103/PhysRevLett.55.1622.

41. P. Lee, A. D. Stone, and H. Fukuyama, "Universal Conductance Fluctuations in Metals: Effects of Finite Temperature, Interactions, and Magnetic Field," *Physical Review B* 35 (1987): 1039, https://doi.org/10.1103/PhysRevB.35.1039.

42. B. L. Altshuler, P. A. Lee, and W. R. Webb *Mesoscopic Phenomena in Solids* (Elsevier, 2012).

43. C. Umbach, S. Washburn, R. Laibowitz, and R. A. Webb, "Magnetoresistance of Small, Quasi-one-dimensional, Normal-metal Rings and Lines," *Physical Review B* 30 (1984): 4048, https://doi.org/10.1103/PhysRevB.30.4048.

44. J. Bird, A. Grassie, M. Lakrimi, K. Hutchings, J. Harris, and C. Foxon, "Conductance Fluctuations and Non-diffusive Motion in GaAs/AlGaAs Heterojunction Wires," *Journal of Physics: Condensed Matter* 2 (1990): 7847, https://doi.org/10.1088/0953-8984/2/38/010.

45. C. Beenakker and H. van Houten, "Quantum Transport in Semiconductor Nanostructures," *Solid State Physics* 44 (1991): 1–228.

46. C. Marcus, A. Rimberg, R. Westervelt, P. Hopkins, and A. Gossard, "Conductance Fluctuations and Chaotic Scattering in Ballistic Microstructures," *Physical Review Letters* 69 (1992): 506, https://doi.org/10.1103/PhysRevLett.69.506.

47. S. Xiong and A. D. Stone, "Universal Conductance Fluctuations in the Presence of Landau Quantization," *Physical Review Letters* 68 (1992): 3757, https://doi.org/10.1103/PhysRevLett.68.3757.

48. D. Maslov and D. Loss, "Edge-state Transport and Conductance Fluctuations in the Metallic Phase of the Quantum Hall Regime," *Physical Review Letters* 71 (1993): 4222, https://doi.org/10.1103/PhysRevLett.71.4222.

49. J. Simmons, H. Wei, L. W. Engel, D. Tsui, and M. Shayegan, "Resistance Fluctuations in Narrow AlGaAs/GaAs Heterostructures: Direct Evidence of Fractional Charge in the Fractional Quantum Hall Effect," *Physical Review Letters* 63 (1989): 1731, https://doi.org/10.1103/PhysRevLett.63.1731.

50. C. Berger, Z. Song, X. Li, et al., "Electronic Confinement and Coherence in Patterned Epitaxial Graphene," *Science* 312 (2006): 1191–1196, https://doi.org/10.1126/science.1125925.

51. H. B. Heersche, P. Jarillo-Herrero, J. B. Oostinga, L. M. Vandersypen, and A. F. Morpurgo, "Bipolar Supercurrent in Graphene," *Nature* 446 (2007): 56–59, https://doi.org/10.1038/nature05555.

52. A. N. Pal, V. Kochat, and A. Ghosh, "Direct Observation of Valley Hybridization and Universal Symmetry of Graphene with Mesoscopic Conductance Fluctuations," *Physical Review Letters* 109 (2012): 196601, https://doi.org/10.1103/PhysRevLett.109.196601.

53. J. Checkelsky, Y. Hor, M.-H. Liu, D.-X. Qu, R. Cava, and N. Ong, "Quantum Interference in Macroscopic Crystals of Nonmetallic Bi2Se3," *Physical Review Letters* 103 (2009): 246601, https://doi.org/10.1103/PhysRevLett.103.246601.

54. S. Matsuo, T. Koyama, K. Shimamura, et al., "Weak Antilocalization and Conductance Fluctuation in a Submicrometer-sized Wire of Epitaxial Bi 2 Se 3," *Physical Review B* 85 (2012): 075440, https://doi.org/10.1103/PhysRevB.85.075440.

55. A. Kandala, A. Richardella, D. Zhang, T. C. Flanagan, and N. Samarth, "Surface-Sensitive Two-Dimensional Magneto-Fingerprint in Mesoscopic Bi 2 Se 3 Channels," *Nano Letters* 13 (2013): 2471–2476, https://doi.org/10.1021/nl4012358.

56. J. Lee, J. Park, J.-H. Lee, J. S. Kim, and H.-J. Lee, "Gate-tuned Differentiation of Surface-conducting States in Bi 1.5 Sb 0.5 Te 1.7 Se 1.3 Topological-insulator Thin Crystals," *Physical Review B* 86 (2012): 245321, https://doi.org/10.1103/PhysRevB.86.245321.

57. M. P. Andersen, L. K. Rodenbach, I. T. Rosen, et al., "Low-damage Electron Beam Lithography for Nanostructures on Bi2Te3-class Topological Insulator Thin Films," *Journal of Applied Physics* 133 (2023): 244301, https://doi.org/10.1063/5.0144726.

58. E. J. Fox, I. T. Rosen, Y. Yang, et al., "Part-per-million Quantization and Current-induced Breakdown of the Quantum Anomalous Hall Effect," *Physical Review B* 98 (2018): 075145, https://doi.org/10.1103/PhysRevB.98.075145.

59. M. Kawamura, R. Yoshimi, A. Tsukazaki, K. S. Takahashi, M. Kawasaki, and Y. Tokura, "Current-Driven Instability of the Quantum Anomalous Hall Effect in Ferromagnetic Topological Insulators," *Physical Review Letters* 119 (2017): 016803, https://doi.org/10.1103/PhysRevLett.119.016803.

60. G. Lippertz, A. Bliesener, A. Uday, L. M. Pereira, A. Taskin, and Y. Ando, "Current-induced Breakdown of the Quantum Anomalous Hall Effect," *Physical Review B* 106 (2022): 045419, https://doi.org/10.1103/PhysRevB.106.045419.

61. B. Skinner, T. Chen, and B. Shklovskii, "Why Is the Bulk Resistivity of Topological Insulators So Small?," *Physical Review Letters* 109 (2012): 176801, https://doi.org/10.1103/PhysRevLett.109.176801.

62. C. Rischau, A. Ubaldini, E. Giannini, and C. J. van Der Beek, "Charge Puddles in a Completely Compensated Topological Insulator," *New Journal of Physics* 18 (2016): 073024, https://doi.org/10.1088/1367-2630/18/7/073024.

63. T. Knispel, W. Jolie, N. Borgwardt, et al., "Charge Puddles in the Bulk and on the Surface of the Topological Insulator $BiSbTeSe_2$ Studied

by Scanning Tunneling Microscopy and Optical Spectroscopy," *Physical Review B* 96 (2017): 195135, https://doi.org/10.1103/PhysRevB.96.195135.

64. H. Beidenkopf, P. Roushan, J. Seo, et al., "Spatial Fluctuations of Helical Dirac Fermions on the Surface of Topological Insulators," *Nature Physics* 7 (2011): 939–943, https://doi.org/10.1038/nphys2108.

65. I. Lee, C. K. Kim, J. Lee, et al., "Imaging Dirac-mass Disorder from Magnetic Dopant Atoms in the Ferromagnetic Topological Insulator $Cr_x(Bi_{0.1}Sb_{0.9})_{2-x}Te_3$," *Proceedings of the National Academy of Sciences* 112 (2015): 1316–1321, https://doi.org/10.1073/pnas.1424322112.

66. G. Ferguson, R. Xiao, A. R. Richardella, D. Low, N. Samarth, and K. C. Nowack, "Direct Visualization of Electronic Transport in a Quantum Anomalous Hall Insulator," *Nature Materials* 22 (2023): 1100–1105, https://doi.org/10.1038/s41563-023-01622-0.

67. M. Allen, Y. Cui, E. Y. Ma, et al., "Visualization of an Axion Insulating state at the Transition between 2 Chiral Quantum Anomalous Hall States," *Proceedings of the National Academy of Sciences* 116 (2019): 14511–14515, https://doi.org/10.1073/pnas.1818255116.

Supporting Information

Additional supporting information can be found online in the Supporting Information section.

Supporting File: adma71985-sup-0001-SuppMat.docx